scientific reports

Check for updates

OPEN

Mechanical mechanism analysis of rockburst in deep-buried tunnel with high in-situ stress

Chao Zhou[1,2,3], Zhihong Dong[1]✉, Chunhua Zhou[1], Ping Fu[1] & Sheng Luo[1]

The Qinling water conveyance tunnel has a large buried depth and high in-situ stress level, and rockburst disasters frequently occurred during excavation. In order to find out the mechanical mechanism of rockburst, the research work in this paper is as follows: (1) In-situ three-dimensional hydraulic fracturing method was used to measure the in-situ stress of the deep buried tunnel crossing the ridge. (2) Based on the measured in-situ stress results, the stress distribution characteristics of the tunnel crossing the ridge were obtained by the multiple linear regression method, and the rockburst tendency during construction was predicted. (3) A three-dimensional numerical model of tunnel excavation was established to analyze the dynamic adjustment characteristics of the surrounding rock stress and elastic strain energy during TBM excavation, and to clarify the mechanical mechanism of rockburst. The research results show that the maximum principal stress of the deep-buried tunnel crossing the ridge of Qinling is 40–66 MPa, which belongs to extremely high in-situ stress level, and medium-strong rockburst may occur during excavation. In the process of TBM excavation, the stress of the surrounding rock in the range of 2.6 times the diameter of the tunnel before and after the working face is adjusted violently, and the concentrated zones after the stress redistribution are mainly distributed in the arch roof and arch bottom, and the stress concentration coefficient can reach 2.06. The arch roof, arch waist, and arch bottom are susceptible to immediate rockburst due to stress transient unloading at the moment of excavation. After the elastic strain energy of the surrounding rock at the arch roof and the arch bottom is released and accumulated, it is easy to cause time delayed rockburst, and the depth of the rockburst pit can reach 3.5 m, which is consistent with the rockburst phenomenon in the field.

Keywords Deep-buried tunnel, In-situ stress, Rockburst, Stress redistribution, Elastic strain energy

The excavation of underground caverns is actually a complex physical and mechanical process of dynamically adjusting the stress balance of the original rock. The excavation unloading breaks the initial stress field equilibrium state of the original rock. Due to the influence of disturbance, the surrounding rock readjusts the stress to produce a secondary stress field or a disturbed stress field to achieve a new stress equilibrium[1–4]. In this process of stress redistribution, the stress of the hard and brittle surrounding cave walls in high stress environment is differentiated, and the elastic strain energy stored in the rock mass is suddenly released, leading to rockburst geological disasters such as bursting, loosening, spalling, ejection and even throwing[5–8]. Due to its randomness, suddenness and destructiveness, rockburst seriously threatens the construction of the project, and the inoculation mechanism in the process of surrounding rock stress adjustment is still unclear. Therefore, it is necessary to deeply study the influence of the surrounding rock disturbance on the triggering effect of rockburst.

In recent years, scholars have deeply studied the mechanical mechanism of rockburst. There are many factors that affect rockburst, including microscopic aspects such as rock mineral composition and rock grain properties, and macroscopic aspects such as temperature, rock mass conditions, stress conditions, excavation methods, and loading and unloading rates. At the microscopic level, Liu et al.[9] and He et al.[10] explored the rockburst mechanism from the perspective of rock mineral cementation type, grain properties and other microstructures. He et al.[11] and Fan et al.[12–15] analyzed the destruction characteristics of solid microstructure under conditions such as thermal–mechanical coupling, high stress and high strain rate from the perspective of crystal structure. Bai

[1]Key Laboratory of Geotechnical Mechanics and Engineering of Ministry of Water Resources, Yangtze River Scientific Research Institute, Wuhan 430010, Hubei, China. [2]State Key Laboratory of Water Resources Engineering and Management, Wuhan University, Wuhan 430072, Hubei, China. [3]Key Laboratory of Rock Mechanics in Hydraulic Structural Engineering, Ministry of Education, Wuhan University, Wuhan 430072, China. ✉email: 14968857@qq.com

et al.[16,17], Tian et al.[18] and Fan et al.[19] analyzed the plastic deformation characteristics of the crystal structure of solid materials under dynamic conditions. Liu et al.[20] and Fan et al.[21–25] studied the nonequilibrium evolution characteristics of microstructures driven by energy fields in complex material systems. Zhao et al.[26] studied the influence of microstructural characteristics such as mineral composition and grain size on rockburst prediction indicators W_{et} and B. At the macroscopic level, Si et al.[27] revealed the mechanism of the influence of temperature thermal effect on rockburst through true triaxial tests on granite cubes with a circular through hole. Si et al.[28] used true triaxial tests to study the influence of lithology and bedding angle on the failure behavior of the surrounding rock of a "D" type tunnel. Su et al.[29] conducted a model test on the tunnel working face with a granite non-circular hole specimen to investigate the effect of tunnel axial stress and the rock column thickness on the working face rockburst during bidirectional excavation, and explained the process of rockburst formation on the tunnel working face in terms of the local energy release rate LERR index by numerical simulation. Wu et al.[30] studied the characteristics and mechanism of strain-induced rockburst failure under different pre-stress conditions using a new biaxial Hopkinson equipment. Li et al.[31] explained the energy source of strain rockburst and energy conversion in the process of rockburst with conceptual theoretical model, and distinguished the dissipated energy and released energy of surrounding rock during tunnel excavation by numerical simulation. Zhu et al.[32] studied the failure characteristics and the distribution of stress field and energy field of the surrounding rock after tunnel excavation under different in-situ stress levels by discrete element method, and determined the rockburst tendency by multiple indexes such as rock characteristics, rock integrity and releasable elastic strain energy of the surrounding rock. Qiu et al.[33] inverted the in-situ stress field in the engineering area based on the measured in-situ stress data, and combined with the advanced geological exploration data to predict the rockburst intensity in front of the working face. Liu et al.[34] realized the monitoring and prediction of rockburst by analyzing the characteristics of microseismic activity during the excavation of deep-buried tunnel with high in-situ stress. The above researches have carried out a series of studies on the mechanism of rockburst from micro and macro levels, but its understanding is not comprehensive enough. There are few studies on the dynamic process of elastic strain energy release and accumulation of surrounding rock caused by stress redistribution during tunnel excavation.

In this paper, aiming at the problem of rockburst disaster in the construction process of the Qinling water conveyance tunnel of the Hanjiang-to-Weihe River Diversion Project, firstly, the three-dimensional hydraulic fracturing method is used to measure the in-situ stress of the main ridge section to understand the background in-situ stress field. Secondly, the stress distribution characteristics of the tunnel crossing the ridge are obtained by regression inversion according to the measured in-situ stress results, and the rockburst tendency during the construction period is preliminarily predicted according to the strength-stress ratio. Finally, a numerical model is established to simulate the excavation process of the tunnel, and the dynamic adjustment process of the stress and elastic strain energy of the surrounding rock is analyzed. The rockburst tendency is predicted by the energy index and compared with the rockburst in the field.

Rockburst criterion

The formation mechanism of rockburst is extremely complicated, and scholars at home and abroad have no unified understanding of the classification and occurrence mechanism of rockburst. Based on laboratory research and field investigation, scholars from all over the world have proposed various rockburst discrimination indexes, mainly including single-index discrimination method such as lithology, critical buried depth, stress and energy, and multi-index comprehensive discrimination method[35,36]. Each criterion has its own application conditions, with certain limitations, but the root causes are related to the geological conditions, stress, energy and physical and mechanical properties of the rock mass where the rockburst occurs. Therefore, this paper discriminates rockburst from stress and energy.

Stress criterion of rockburst

The in-situ stress is the force source condition of the rockburst, and the maximum principal stress controls the area and energy of the rockburst. Tunnel excavation causes stress redistribution in the surrounding rock, and the surrounding rock stress in the stress concentration area often exceeds the critical stress of rockburst, and then rockbusrt occurs. According to the ratio of saturated uniaxial compressive strength σ_c to maximum initial principal stress σ_m, rockburst are classified in the Code for Engineering Geological Investigation of Water Resources and Hydropower[37], as follows:

$$\begin{cases} 4 \le \sigma_c / \sigma_m \le 7 & \text{Light rockburst} \\ 2 \le \sigma_c / \sigma_m \le 4 & \text{Medium rockburst} \\ 1 \le \sigma_c / \sigma_m \le 2 & \text{Strong rockburst} \\ \sigma_c / \sigma_m < 1 & \text{Extremely strong rockburst} \end{cases}$$

This criterion can be used to predict the rockburst during tunnel construction according to the in-situ stress field and rock mass properties.

Energy criterion of rockburst

If the deep-buried tunnel is not excavated, a certain degree of elastic strain energy will accumulate in the rock mass. Excavation will result in the release and accumulation of strain energy in the surrounding rock. When the energy exceeds the energy storage of the rock mass, the strain energy will be suddenly released and may cause a rockburst. Chen et al.[38] conducted pre-peak and post-peak unloading confining pressure tests on granite under different confining pressures, different control methods and different unloading rates, analyzed the characteristics

of energy dissipation and energy release in the process of rock deformation and failure, and proposed a simple and practical energy discriminant index that can quantitatively predict rockburst in numerical simulation:

$$\begin{cases} U_e/U_0 < 0.3 & \text{Light rockburst} \\ 0.3 \le U_e/U_0 < 0.5 & \text{Medium rockburst} \\ 0.5 \le U_e/U_0 < 0.7 & \text{Strong rockburst} \\ 0.7 \le U_e/U_0 & \text{Extremely strong rockburst} \end{cases}$$

where *Ue* is the elastic releasable strain energy of the rock mass element, and U_0 is the ultimate energy storage of the rock mass element under specific confining pressure, which can be calculated by the following formulas respectively:

$$U_e = \frac{\sigma_1^2 + \sigma_2^2 + \sigma_3^2 - 2\nu(\sigma_1\sigma_2 + \sigma_2\sigma_3 + \sigma_1\sigma_3)}{2E} \quad (1)$$

$$U_0 = \frac{\sigma_c^3}{2E(\sigma_1 - \sigma_3)} \quad (2)$$

where σ_1, σ_2 and σ_3 are the first, second and third principal stresses of the element respectively after tunnel excavation; σ_c is uniaxial compressive strength of rock mass; E is Young's modulus; ν is Poisson 's ratio.

Project Overview

Engineering background

The Hanjiang-to-Weihe River Diversion Project is a South-to-North Water Diversion Project in Shanxi Province, China, which consists of a water diversion project and a water transmission and distribution project. The water diversion project includes the Golden Gorge Water Conservancy Hub, the Sanhekou Water Conservancy Hub and the Qinling Water Conveyance Tunnel crossing the Qinling Mountains with a total length of 98.3 km and a maximum buried depth of about 2012 m. The total length of the tunnel crossing the ridge is 81.779 km, of which 39.08 km through the main ridge of Qinling Mountains is constructed by TBM, and the section of the tunnel is a circle with a diameter of 8.02 m.

In this paper, the total length of K36 + 000–K49 + 000 in the study area is 13 km with the buried depth of more than 800 m. The surrounding rocks of the tunnel in this area are granite, diorite and meta sandstone, in which the granite and diorite sections are slightly weathered to unweathered and dominated by Class II surrounding rocks, while the meta sandstone section is weakly weathered to slightly weathered and dominated by Class III surrounding rocks. The QF4 and f8 fault fracture zones and influence zones are distributed in the diorite and meta sandstone section, and the tectonic action is strong. Figure 1 is the geological profile of the ridge-crossing section. The geological conditions of the deep-buried tunnel section are complicated, and the surrounding rock is in the complex mechanical environment of "three highs and one disturbance" during excavation, which makes the rockburst disaster problem prominent.

Characteristics of rockburst during construction period

From March 28, 2019 to April 8, 2020, the TBM excavation work of K39 + 550–K40 + 850 (1288 m) was completed on the south side of the ridge. The buried depth of this tunnel section ranges from 1304 to 1510 m. A total of 720 rockbursts occurred during excavation, including 146 light rockbursts, 216 medium rockbursts and 358 strong rockbursts. Figure 2 is the statistic of the number of rockbursts of different grades at different depths and mileages in this tunnel section. It can be seen that the buried depth is different under different rockburst grades, and the rockburst grade is directly proportional to the buried depth. The greater the buried depth, the stronger the rockburst intensity.

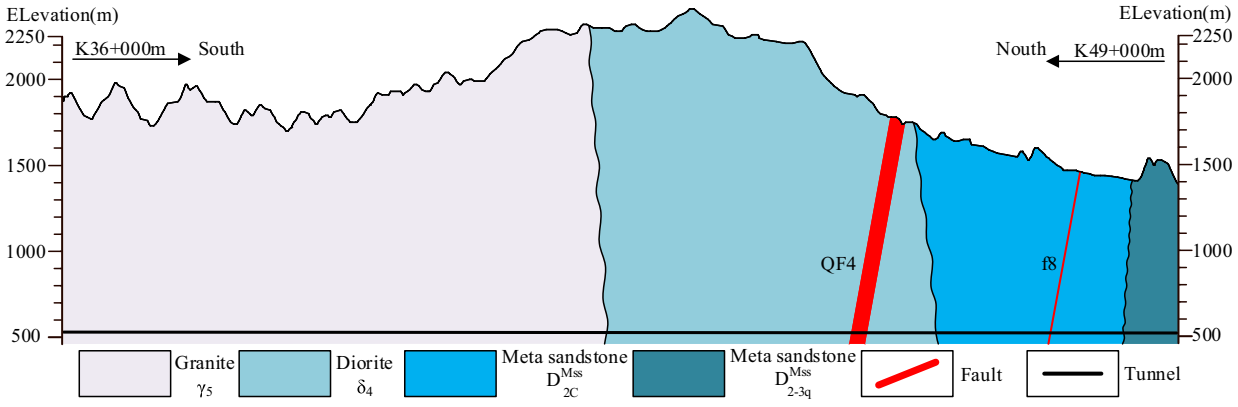

Figure 1. Geological profile of the ridge-crossing section.

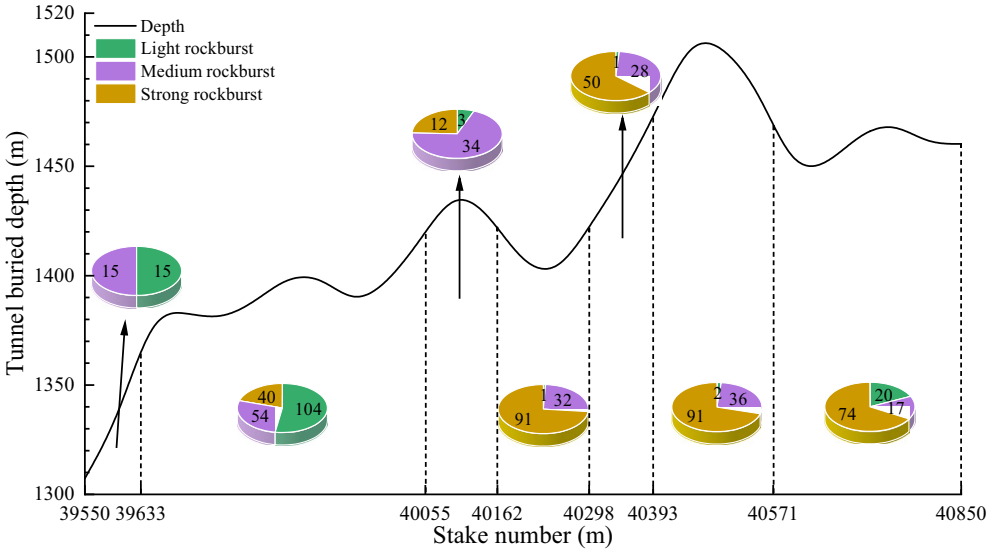

Figure 2. Rockburst statistics.

According to the field statistics, light rockbursts mainly occurred at the arch roof within one times the tunnel diameter from the working face, with fewer side walls and no arch bottom. Moderate and strong rockbursts mainly occurred at the arch roof and shoulder of the tunnel within 2–3 times the tunnel diameter from the working face, accounting for about 66% of the total number of rockbursts. The probability of occurrence is about 20% at the arch waist and occasionally at the right arch bottom. The damage depth of surrounding rock caused by rockburst is 0.1–3.8 m, and the shape of the pit is mainly triangular and conical. From the geological conditions of the on-site rockburst location, rockbursts mostly occurred in intact hard surrounding rock, and the compressive strength of the surrounding rock is mainly between 100 and 200 MPa. When the compressive strength is less than 100 MPa, rockburst rarely occurred. The development degree and direction of joints are closely related to rockbursts.

Study on the in situ stress in the ridge cross section

In-situ stress measurement

In-situ stress and excavation disturbance are two basic factors of rock burst during tunnel excavation[39,40]. Therefore, the research team conducted three-dimensional hydraulic fracturing in-situ stress tests at K38 + 850 (buried depth of about 1300 m) in the south of the ridge granite section and K46 + 190 (buried depth of about 1170 m) in the north of the ridge meta sandstone section of the Qinling deep buried tunnel. The three-dimensional hydraulic fracturing method does not assume that the borehole axis is one of the principal stress directions, and thus a more accurate three-dimensional stress state can be obtained than the results obtained by the conventional hydraulic fracturing method. The principle of the method is to conduct conventional hydraulic fracturing tests by using three boreholes in different directions to form a three-dimensional in-situ stress measurement section, and then obtain the three-dimensional in-situ stress values and directions by the coordinate transformation of the stress components and the solving of linear algebraic equations. The detailed principle of the 3D hydraulic fracturing method is described by Zhou et al.[41]. The boreholes layout is shown in Fig. 3. The field test condition and typical fracturing curve are shown in Fig. 4.

Due to space limitations and for ease of later application, only the results of the vertical boreholes (Table 1) and the final three-dimensional results (Table 2) are presented in this paper. It can be seen that the horizontal principal stress obtained by the three-dimensional hydraulic fracturing method is basically consistent with that obtained by the two-dimensional hydraulic fracturing method for vertical boreholes, which confirms the reliability of the test results. The maximum principal stress of the Qinling tunnel crossing the ridge reaches 62.8–65.0 MPa, which is an extremely high stress level. In terms of horizontal principal stresses, the principal stresses of the

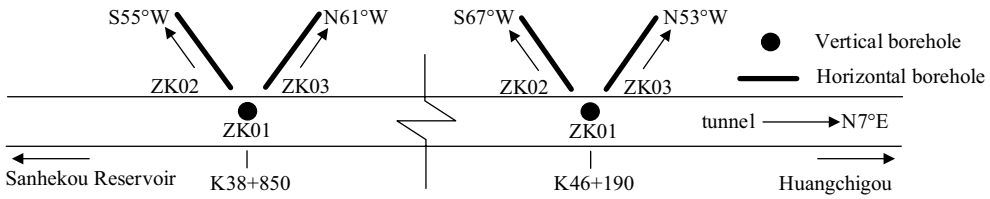

Figure 3. Boreholes layout.

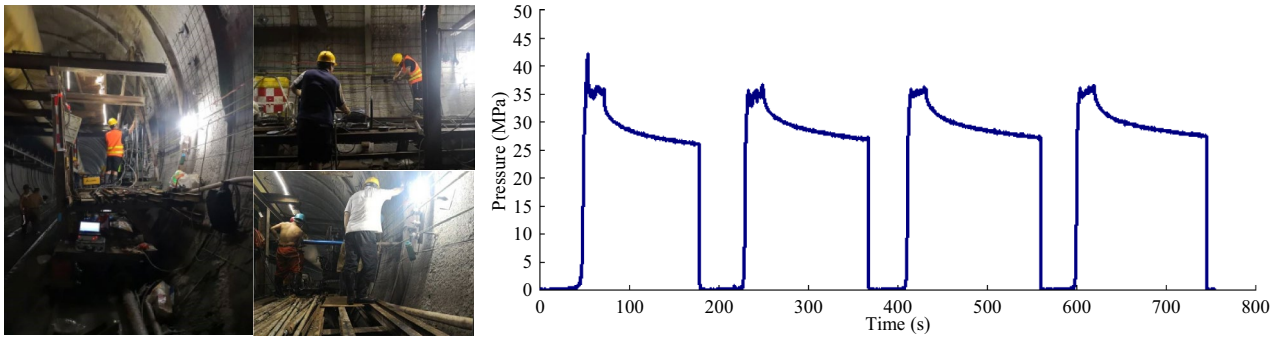

(a) Field test condition (b) Typical fracturing curve

Figure 4. Field test condition and typical fracturing curve.

Borhole	Depth/m	σ_H/MPa	σ_h/MPa	σ_Z/MPa	λ_H	λ_h	α_H/°
K38 + 850 ZK01	10.0	40.6	22.2	33.3	1.2	0.7	
	14.1	42.8	22.7	33.4	1.3	0.7	
	17.7	49.1	27.4	33.5	1.5	0.8	
	20.1	53.6	28.5	33.5	1.6	0.9	117°
	24.4	54.2	28.6	33.7	1.6	0.8	
	27.8	53.1	28.0	33.7	1.6	0.8	103°
K46 + 190 ZK01	12.8	52.4	33.1	31.9	1.6	1.0	86°
	14.7	62.3	38.3	32.0	1.9	1.2	
	16.3	57.3	34.3	32.0	1.8	1.1	
	17.9*	34.3	27.3	32.1	1.8	0.9	
	19.5	59.7	36.3	32.1	1.9	1.1	
	21.1	65.5	38.2	32.2	2.0	1.2	81°
	25.2	62.7	34.8	32.3	1.9	1.1	

Table 1. In-situ stress test results from vertical boreholes. σ_H: maximum horizontal principal stress; σ_h: minimum horizontal principal stress; σ_Z: self-weight stress; λ_H: maximum horizontal lateral stress factor, $\lambda_H = \sigma_H/\sigma_Z$; λ_h: minimum horizontal lateral stress factor, $\lambda_h = \sigma_h/\sigma_Z$; α_H: maximum horizontal principal stress azimuth.

	Spatial principal stress									Horizontal principal stress		
	σ_1			σ_2			σ_3			σ_H	σ_h	α_H
Experimental position	Value (MPa)	Dip angle (°)	Azimuth angle (°)	Value (MPa)	Dip angle (°)	Azimuth angle (°)	Value (MPa)	Dip angl e °)	Azimuth angle (°)	Value (MPa)	Value (MPa)	Azimuth angle (°)
K38 + 850	62.8	37	276	37.1	25	165	25.5	42	49	51.1	33.2	107
K46 + 190	65.0	9	269	49.6	48	11	26.8	40	172	64.5	36.4	86

Table 2. Three-dimensional in-situ stress test results.

south of the ridge granite section mainly show $\sigma_H > \sigma_Z > \sigma_h$, and the principal stresses of the north of the ridge meta sandstone section mainly show $\sigma_H > \sigma_h \geq \sigma_Z$, both of which are dominated by horizontal tectonic stress. Influenced by the topography and fault structure, the horizontal principal stress direction in the north of the ridge and in the north of the ridge is slightly different. The stress direction in the south of the ridge is mainly NWW, and the stress direction in the north of the ridge is mainly NEE. According to the overall analysis, the stress direction of the Qinling tunnel is generally EW, which is consistent with the characteristics of the second-stage tectonic stress field, where the stress field is dominated by NWW-SEE compression.

Inversion analysis of in-situ stress field

In-situ stress testing is the most direct way to understand the stress field in the engineering area. However, due to factors such as expensive testing costs, test site limitations and complex geological conditions, it is impossible to conduct detailed and extensive testing, and the measurement results at each measuring point can only reflect the local stress field[41]. Therefore, this paper adopts the multivariate linear regression method[42] to invert the

in-situ stress field in the ridge section of the Qinling deep buried tunnel in order to understand the distribution law of the in-situ stress field.

Model and mechanical parameters

The 3D numerical calculation model with a total length of 13 km from K36 + 000 to K49 + 000 in the ridge section of the Qinling tunnel is established, which reflects the main lithology and geological structure in the project area, as shown in Fig. 5. The linear elastic constitutive model is used in the calculation. The calculation parameters of the rock mass are comprehensively selected according to the tunnel investigation test, as shown in Table 3.

Analysis of inversion results

The stress field inversion aims at the initial in-situ stress field in the engineering area, while the measured in-situ stress is measured in the excavated tunnel, and the shallow stress of the surrounding rock is mainly the secondary stress field disturbed by the excavation, so the shallow measuring points cannot be used for stress field inversion. According to the measured results and engineering experience, the undisturbed in-situ stress is about 2 times the diameter of the tunnel, which can be used for the inversion of the initial in-situ stress field. Based on the in-situ stress data from deep measuring points, the initial in-situ stress field in the engineering area of the Qinling tunnel crossing the ridge is obtained by inversion. Figure 6 shows the distribution of maximum and minimum principal stresses of the model obtained by inversion.

Figure 7 shows the comparison between the measured and the calculated values of each measuring point outside the range of 2 times the tunnel diameter of the vertical borehole. The results show that the measured values of each measuring point are in good agreement with the regression calculated values, and the calculated maximum horizontal principal stress direction is close to the measured direction. Therefore, the in-situ stress field obtained by regression is reasonable.

Stress distribution law in the axial direction of the tunnel

In order to understand the stress state of the tunnel, and to provide a reference for the study of rockburst mechanism and engineering design during tunnel construction, the stress values of the tunnel at different positions are obtained by interpolation from the regression results of the in-situ stress field. Figures 8 and 9 show the

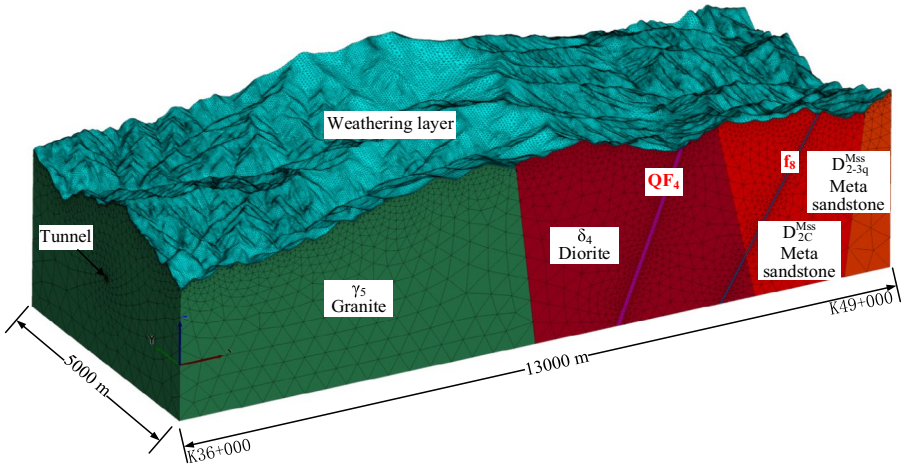

Figure 5. 3D numerical calculation model drawn using Altair 2021 Hypermesh software.

Lithology	Young's modulus (GPa)	Poisson's ratio	Density (kg/m³)	Internal friction angle (°)	Cohesion (MPa)	Tensile strength (MPa)
Granite (γ_5)	37.1	0.2	2660	58	2.4	2.7
Diorite (δ_4)	26.3	0.22	2700	56	2.1	2.4
Meta sandstone(DMss 2C)	20.6	0.25	2640	48	1.5	2
Meta sandstone(DMss 2-3q)	18.7	0.27	2630	44	1.3	1.8
Fault	1.1	0.33	2350	25	0.18	0.1
Weathering layer	0.7	0.4	1950	20	0.1	–

Table 3. Rock mechanical parameters.

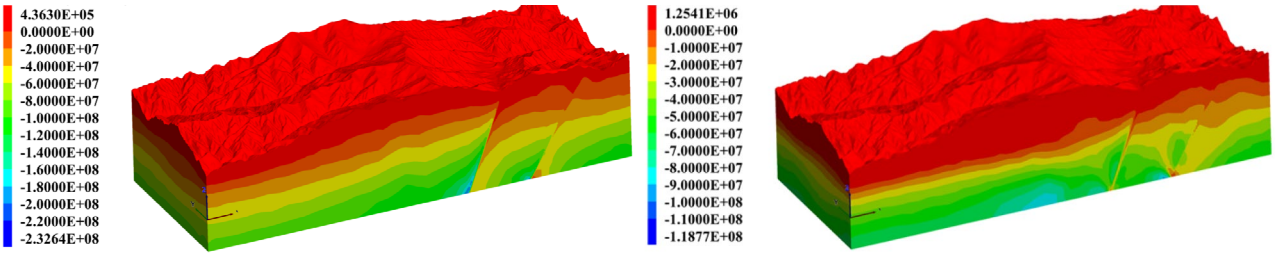

(a) σ_1 (b) σ_3

Figure 6. Model principal stress distribution drawn using ITASCA's FLAC^{3D} 7.0 software(unit: Pa).

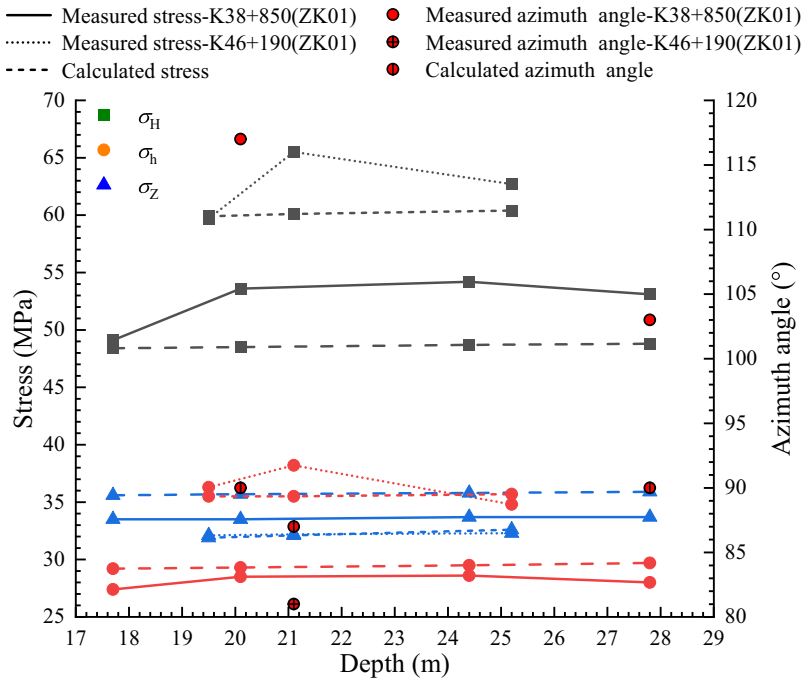

Figure 7. Comparison of measured and calculated values.

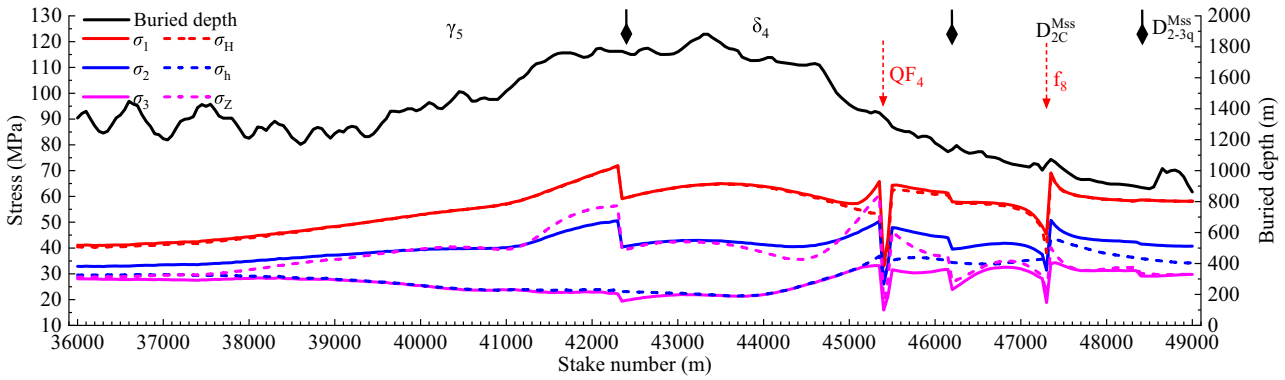

Figure 8. Principal stress distribution law.

distribution of principal stresses and buried depth, lateral pressure coefficients and azimuth angles of maximum horizontal principal stresses in relation to the stake number on the tunnel axis in the Qinling tunnel crossing the ridge, respectively.

It can be seen that the stress at the lithologic boundary and the fault is significantly different, and the stress in the fault influence zone is significantly lower than that in the complete rock mass. The first principal stress of the tunnel is 32.8–71.9 MPa, the second principal stress is 25.9–50.7 MPa, and the third principal stress is

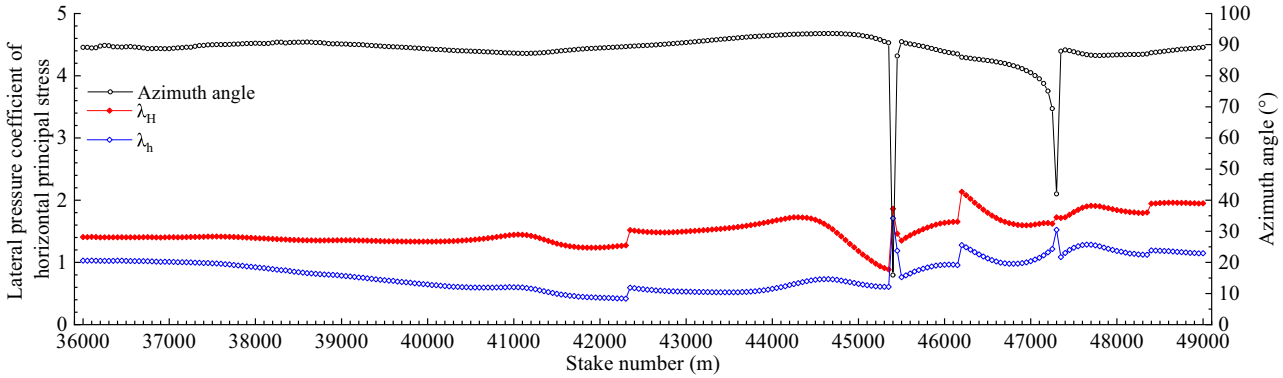

Figure 9. Lateral pressure coefficient and azimuthal angle distribution law.

15.9–34.3 MPa. The maximum horizontal principal stress is 31.7–71.8 MPa, the minimum horizontal principal stress is 21.4–43.5 MPa and the self-weight stress is 17.0–60.7 MPa. The stress field of the tunnel is mainly horizontal stress, and the lateral pressure coefficients of the maximum and minimum horizontal principal stress are distributed in 0.88–2.14 and 0.41–1.71, respectively, mainly concentrated in 1.4–1.7 and 0.6–1.2, respectively. The buried depth of the granite and diorite tunnel section is greater than 1100 m, and the horizontal principal stress is $\sigma_H > \sigma_Z > \sigma_h$. The buried depth of the meta sandstone tunnel section is less than 1100 m, and the horizontal principal stress is $\sigma_H > \sigma_h > \sigma_Z$. The maximum horizontal principal stress azimuth angle of the tunnel is concentrated at 85° ~ 95°, which is nearly perpendicular to the tunnel axis, which is unfavorable to the stability of the surrounding rock of the tunnel.

Rockburst tendency during construction period

Based on the σ_c/σ_m rockburst criterion, the rockburst tendency of the Qinling tunnel crossing the ridge during the construction period was predicted. The saturated uniaxial compressive strength of granite (γ_5), diorite (δ_4), meta sandstone (DMss 2C) and meta sandstone (DMss 2-3q) is 150 MPa, 125 MPa, 120 MPa and 115 MPa respectively, and σ_c/σ_m was calculated along the tunnel. The rockburst tendency during construction period along the tunnel is shown in Fig. 10.

It can be seen that during the excavation of the tunnel construction, there is a possibility of medium rockburst in the granite tunnel section on the south side of the ridge, and the probability of strong rockburst gradually increases with the increase of the buried depth of the tunnel. In the diorite tunnel section, if the buried depth is greater than about 1500 m, strong rockburst may occur. If the buried depth is less than about 1500 m, medium rockburst may occur. In addition, strong rockburst may occur in the tunnel section near the QF4 fault influence zone. Medium rockburst may occur in the tunnel section of meta sandstone (DMss 2C), while strong rockburst may occur near the f8 fault influence zone. Strong rockburst may occur in the tunnel section of meta sandstone (DMss 2-3q).

Numerical simulation analysis of TBM excavation in rockburst tunnel section

Model and monitoring points

A three-dimensional numerical model of the tunnel excavation was established using the example of the K39 + 550–K40 + 850 rockburst tunnel section with an average buried depth of 1400 m in the granite tunnel section on the south side of the ridge in "Characteristics of rockburst during construction period" section. The size of the model is 100 m × 60 m × 100 m (X × Y × Z), and the excavation diameter of the tunnel is 8.02 m, as shown in Fig. 11a. The X-axis is the horizontal axis perpendicular to the tunnel axis, the Y-axis is along the direction

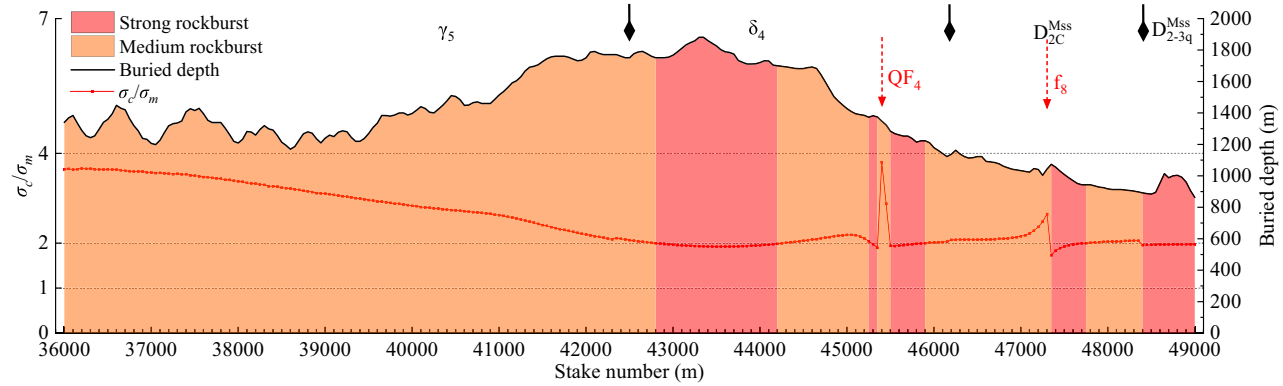

Figure 10. Rockburst tendency during construction period along the tunnel.

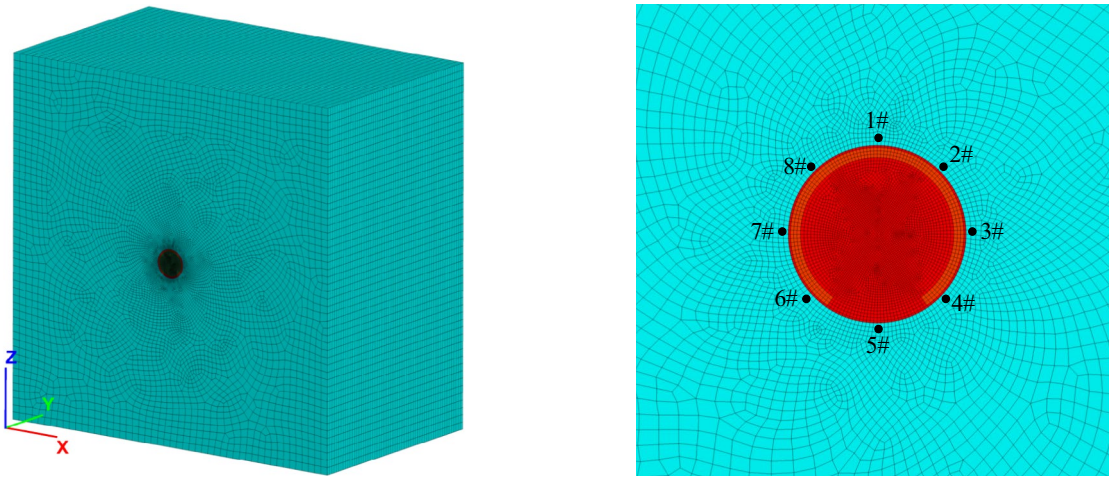

(a) Calculation model (b) Monitoring points

Figure 11. Calculation model and monitoring points.

of the tunnel axis, and the Z-axis is straight up. In the process of tunnel excavation, eight measurement points, including the arch roof (1#), the right arch shoulder (2#), the right arch waist (3#), the right arch foot (4#), the arch bottom (5#), the left arch foot (6#), the left arch waist (7#), the left arch shoulder (8#) on the monitoring section Y = 30 m in the central part of the model are monitored, and the arrangement of the monitoring points is shown in Fig. 11b.

The Mohr–Coulomb constitutive model is used in the calculation, and the model parameters are shown in Table 3. The initial stress field of the model is interpolated and balanced directly from the overall in-situ stress field obtained by inversion. Then, the continuous construction process of the TBM excavation is simulated, with each excavation step of 1 m.

Dynamic adjustment characteristics of the surrounding rock stress

Figure 12a shows the stress redistribution of the surrounding rock after tunnel excavation, and Fig. 12b shows the stress distribution at different distances from the tunnel wall in the radial OA and OB directions. It can be seen that after tunnel excavation, the surrounding rock stress is redistributed, and the adjustment range is about 3.5 times the diameter of the tunnel. The surrounding rock stress is basically symmetrically distributed, and the angle between the symmetry plane and the vertical direction is about 5°. The surrounding rock stress in the range of about 0.3 m around the tunnel is apparently released, forming a loose circle. The arch roof and arch bottom of the tunnel form stress concentration zones (the maximum principal stress can reach 96.8 MPa) in the depth

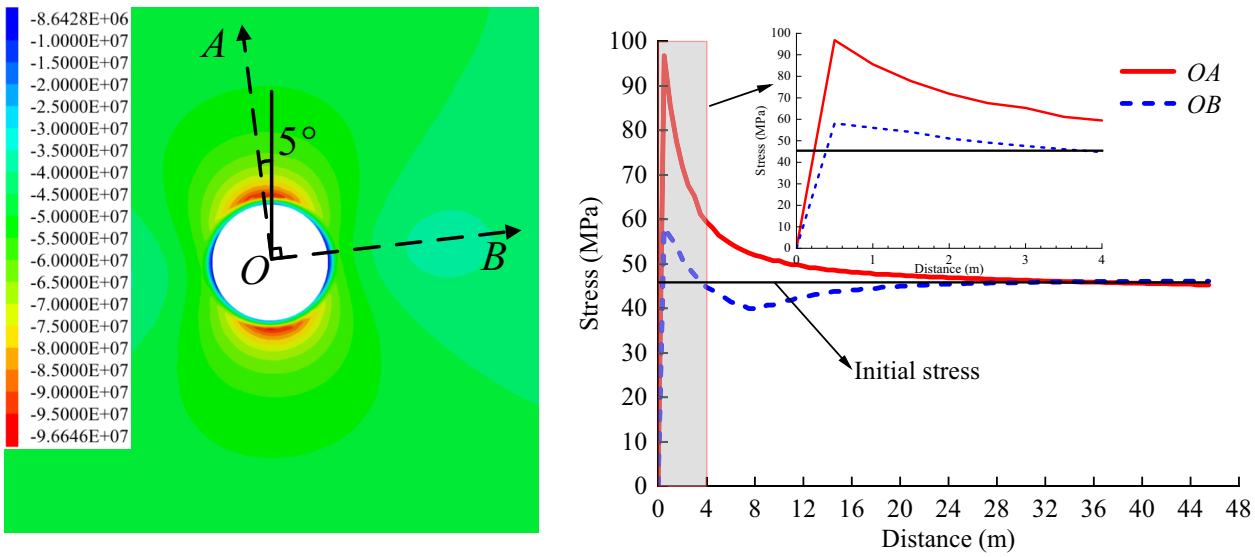

(a) Maximum principal stress distribution (unit: Pa)

(b) Surrounding rock Stress distribution at different distances from the tunnel wall

Figure 12. Surrounding rock stress distribution.

range of 0.3–28 m from the tunnel wall, of which the range of 0.3–5 m is the most obvious. The left and right side walls of the tunnel form stress concentration zones (the maximum principal stress can reach 58.1 MPa) in the depth range of 0.3–3.5 m, and stress unloading zones are formed in the depth range of 3.5–24 m.

Figure 13 shows the stress dynamic variation law of each monitoring point on the monitoring section during TBM excavation. Due to the symmetry of the surrounding rock stress distribution, only 1#–5# measuring points are analyzed here. The principal stress states of σ_1, σ_2, and σ_3 under initial stress are basically the same as those of σ_X, σ_Z, and σ_Y respectively, that is, the direction of maximum principal stress σ_1 is perpendicular to the tunnel axis, the direction of intermediate principal stress σ_2 is basically vertical, and the direction of minimum principal

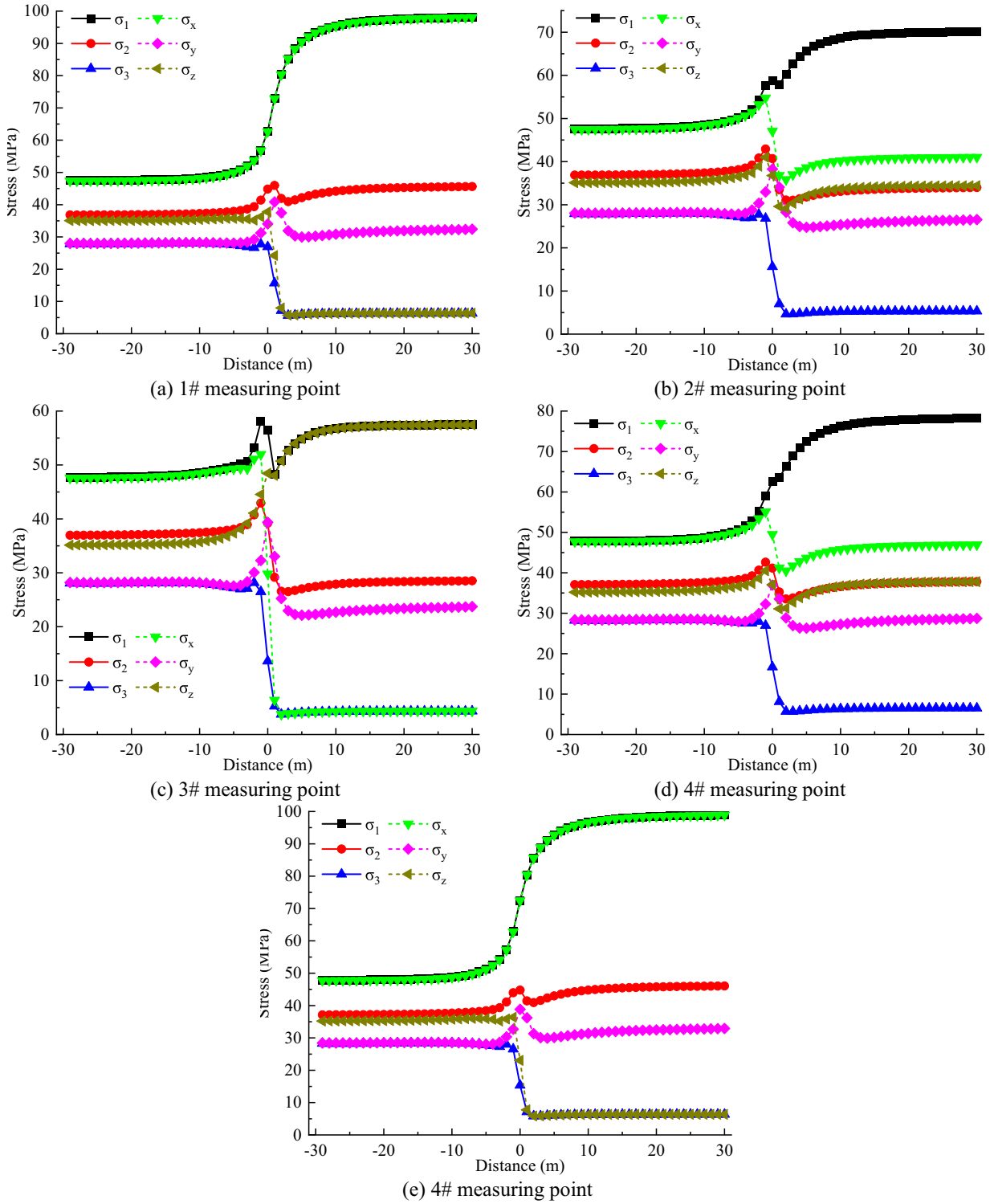

Figure 13. Stress dynamics change law at each monitoring point.

stress σ_3 is the tunnel axis. During the TBM excavation, stress adjustment occurred in the range of approximately 3.7 times the tunnel diameter (− 15 to 15 m) before and after the working face.

As can be seen from Fig. 13a,e, the stress evolution law of the arch roof and arch bottom is basically the same. As the working face is close to the monitoring section, σ_1 and σ_2 gradually increase, while σ_3 first decreases and then increases. As the working face passes through the monitoring section and moves far away, σ_1 continues to increase until stability is reached, and σ_2, σ_3 first decrease and then increase until stability is reached. After the surrounding rock stress is stabilized, σ_1 shows obvious stress concentration, σ_2 stress level is slightly increased but not significant, and σ_3 shows obvious stress unloading effect, and the quantities of σ_1, σ_2, and σ_3 are 2.06, 1.24, and 0.22 times of the initial stress state, respectively. The values of σ_1 and σ_3 after adjustment for the surrounding rock stress are consistent with the values of σ_X, and σ_Z, respectively, and the difference between σ_2 and σ_Y is about 10 MPa. It indicates that the stress directions of σ_2 and σ_3 at the arc roof and arch bottom was changed, the stress direction of σ_2 was changed from the vertical to a small angle intersecting with the tunnel axis, and the stress direction of σ_3 was changed from the tunnel axis to the vertical.

As can be seen from Fig. 13b,d, the stress evolution law of the arch shoulder and arch foot is basically the same except for the magnitude. As the working face is close to the monitoring section, σ_1 and σ_2 gradually increase, while σ_3 first decreases and then increases. As the working face passes through the monitoring section and moves far away, σ_1, σ_2, and σ_3 first decrease and then increase until stability is reached. After the surrounding rock stress is stabilized, σ_1 shows obvious stress concentration, σ_2 and σ_3 shows obvious stress unloading effect. The quantities of σ_1, σ_2, and σ_3 of the arch shoulder are 1.47, 0.92, and 0.19 times of the initial stress state, and the quantities of σ_1, σ_2, and σ_3 of the arch shoulder are 1.64, 1.02, and 0.23 times of the initial stress state. The values of σ_2 and σ_Z after adjustment for the surrounding rock stress are consistent, and the values of σ_1 and σ_2 are different from those of σ_1 and σ_2, respectively, but the magnitude relationships of σ_X, σ_Y, and σ_Z are still consistent with the initial stress state. It indicates that the principal stress directions of the arch shoulder and arch foot did not change much after the stress redistribution of the surrounding rock.

From Fig. 13c, it can be seen that as the working face is close to the monitoring section, σ_1 and σ_2 gradually increase at the arch waist, while σ_3 first decreases and then increases. As the working face passes through the monitoring section and moves far away, σ_1, σ_2, and σ_3 first decrease and then increase until stability is reached. After the surrounding rock stress is stabilized, σ_1 shows obvious stress concentration, σ_2 and σ_3 shows obvious stress unloading effect, and the quantities of σ_1, σ_2, and σ_3 are 1.21, 0.77, and 0.15 times of the initial stress state, respectively. The values of σ_1 and σ_3 after adjustment for the surrounding rock stress are consistent with the values of σ_Z, and σ_X, respectively, and the difference between σ_2 and σ_Y is about 7 MPa. It indicates that the stress directions at the arc waist was changed, the stress direction of σ_1 was changed from the perpendicular to the tunnel axis to the vertical, the stress direction of σ_2 was changed from the vertical to a small angle intersecting with the tunnel axis, and the stress direction of σ_3 was changed from the tunnel axis to the perpendicular to the tunnel axis.

Dynamic adjustment characteristics of the strain energy of the surrounding rock

During tunnel excavation, due to the release of confining pressure, the surrounding rock stress is redistributed, resulting in the release and accumulation of elastic strain energy. When the elastic strain energy in a certain part accumulates to the energy storage limit of the rock mass, rockburst may occur. Figure 14 shows the distribution of elastic strain energy of the surrounding rock and the change in elastic strain energy after tunnel excavation.

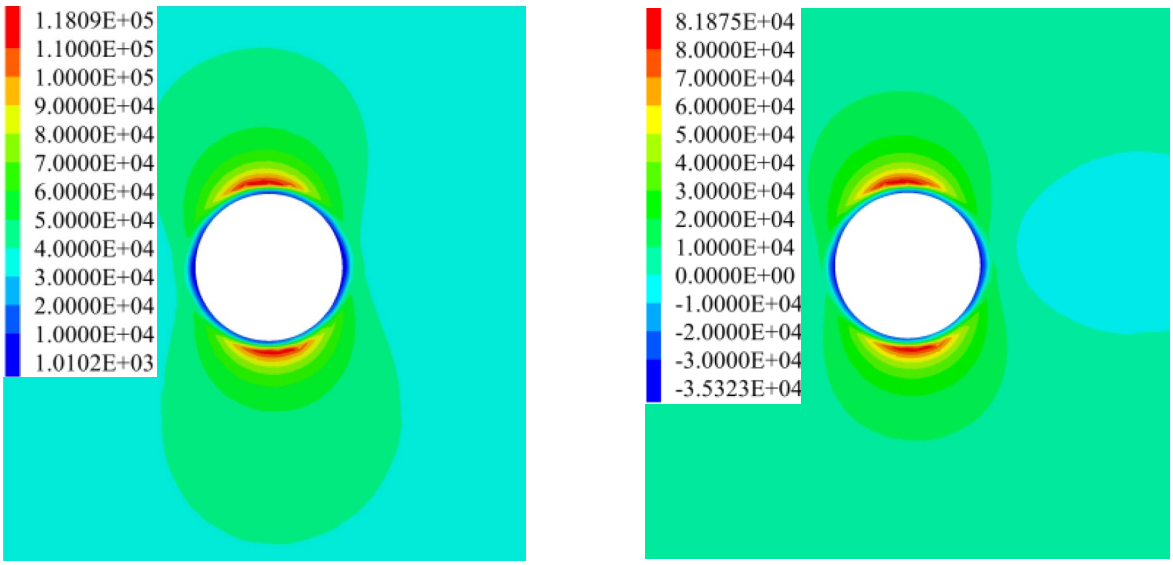

(a) Elastic strain energy distribution after excavation

(b) Change in elastic strain energy before and after excavation

Figure 14. Distribution and change of strain energy after tunnel excavation (unit: J m^3).

Figure 15 shows the variation of elastic strain energy at each monitoring point on the monitoring section with the TBM excavation.

As can be seen from Fig. 14, after excavation, the elastic strain energy of the surrounding rock in the range of 0–0.5 m around the tunnel wall decreases, while the strain energy of other parts increases, and elastic strain energy accumulation zones appear at the arch roof and arch bottom, and the maximum accumulated energy can reach 118.1 kJ/m^3. As can be seen from Fig. 15, as the working face progresses, the elastic strain energy of each measurement point on the monitoring section undergoes a cyclic dynamic adjustment process of release and accumulation, eventually reaching a stable state. For the elastic strain energy stabilized after each excavation step, the elastic strain energy begins to increase significantly at approximately 10 m from the front of the working face. As the working face approaches the monitoring section, the elastic strain energy at each measuring point gradually increases. When the working face reaches the monitoring section, the elastic strain energy at each measuring point increases to the peak value before excavation. When the working face passes through the monitoring section and moves far away, the elastic strain energy of the arch shoulder, arch waist, and arch foot drops sharply at 1 m behind the working face and then continues to increase, while the elastic strain energy of the arch roof and arch bottom continues to increase. The elastic strain energy of each measurement point tends to stabilize when the working face is 20 m away from the monitoring section. The elastic strain energy after excavation stabilization is higher than that before excavation at each measuring point, and the increases of arch bottom and arch roof are the largest, which is 3.49 times that before excavation. The arch foot and arch shoulder are 2.19 times and 1.78 times respectively before excavation. The arch waist is the smallest, which is 1.20 times of that before excavation.

Rockburst mechanical mechanism analysis

The stress state of the surrounding rock of the deep buried tunnel is very complicated. When the tunnel is not excavated, the rock mass is in a three-way and six-sided stress state, while when the tunnel is excavated, the surrounding rock at the surface of the tunnel changes to a three-way and five-sided stress state (Fig. 16), and the deeper part is in a three-way and six-sided stress state, which may lead to rockburst[43,44].

Figure 17 shows the stress path changes at each monitoring point on the monitoring section during tunnel excavation. It can be seen that the stress state at each point is constantly adjusted closer to the strength envelope as the excavation step progresses. From Fig. 17a, the arch roof, arch waist and arch bottom have stress transient unloading at the moment of excavation, and the rock mass element has yielded, which is prone to occur immediate rockburst at this time, and then the stress state is readjusted. From the stress state after each excavation step of the tunnel (Fig. 17b), when the working face reaches the monitoring surface, except for the arch roof, the stress state of the other four monitoring points is close to the strength envelope. When the working face passes 2–3 m through the monitoring section, the stress state of all measuring points reaches the vicinity of the strength envelope, and then the stress state develops basically parallel to the strength envelope. The stress state of the arch roof and arch bottom has basically reached a critical state, and rockburst is most likely to occur after an external disturbance, which is a time delayed rockburst.

According to the variation law of the stress path of the surrounding rock during tunnel excavation, the potential risk area of rockburst can be identified, and the force source conditions of rockburst can be found out, but it is difficult to determine the rockburst intensity. According to the rockburst energy criterion in "Energy criterion of rockburst" Section, the distribution of the ratio U_e/U_0 between the elastic strain energy storage U_e and the ultimate energy storage U_0 of the surrounding rock was obtained, as shown in Fig. 18a. It can be seen that the maximum value of U_e/U_0 at the arch roof and arch bottom of the tunnel can reach 0.54, and there is a possibility of strong rockburst. The distance between the critical point of the strong rockburst and the tunnel surface is about 3.6 m, which is consistent with the depth of rockburst pit of 0.1–3.8 m according to the field statistics (Fig. 18b).

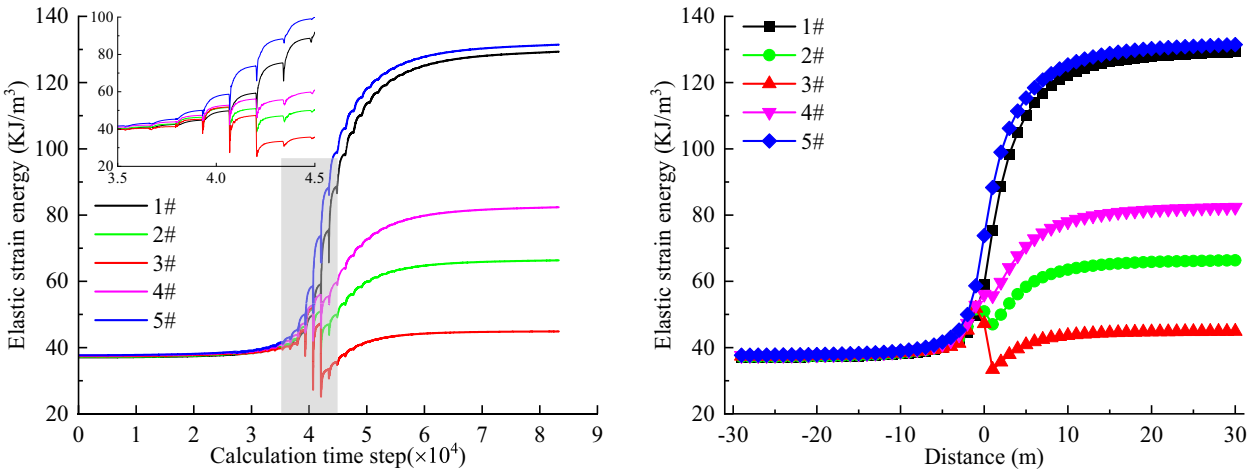

(a) History of elastic strain energy change (b) Variation of elastic strain energy with excavation step

Figure 15. Evolution law of elastic strain energy at monitoring points.

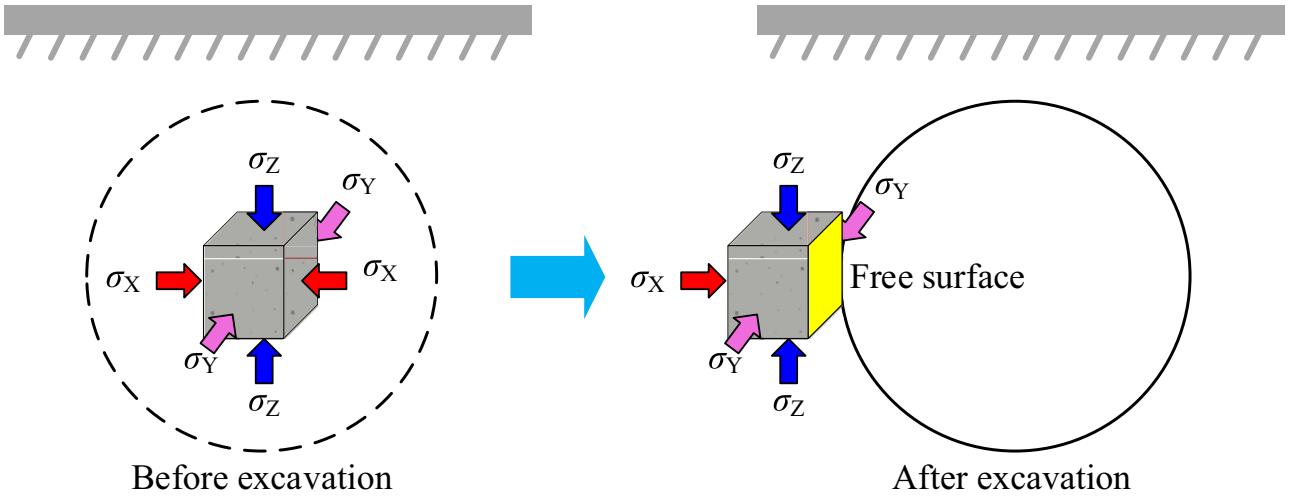

Figure 16. Stress state of rock mass before and after excavation.

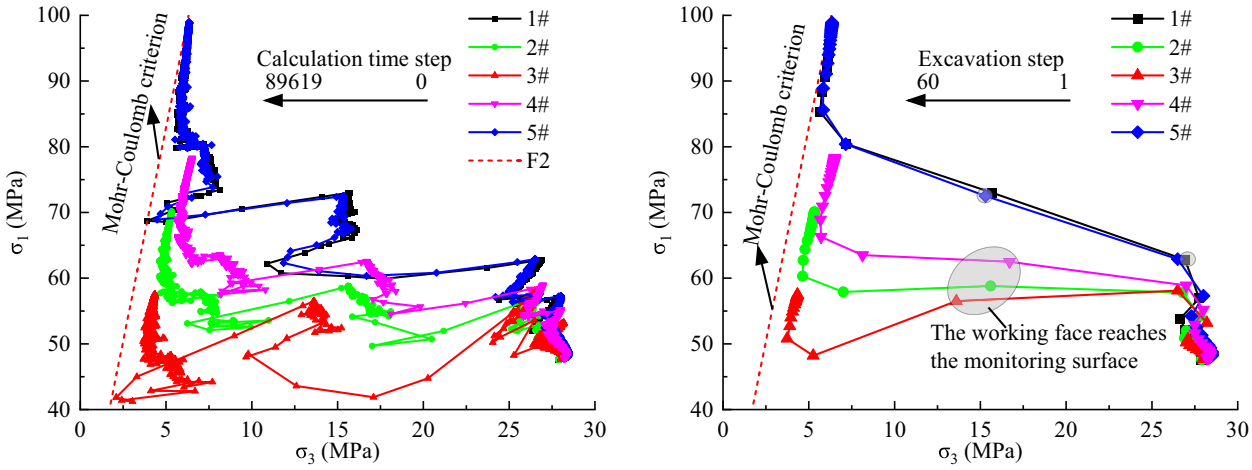

(a) History of stress path change

(b) Stress path change after each excavation

Figure 17. Stress path change at monitoring points during tunnel excavation.

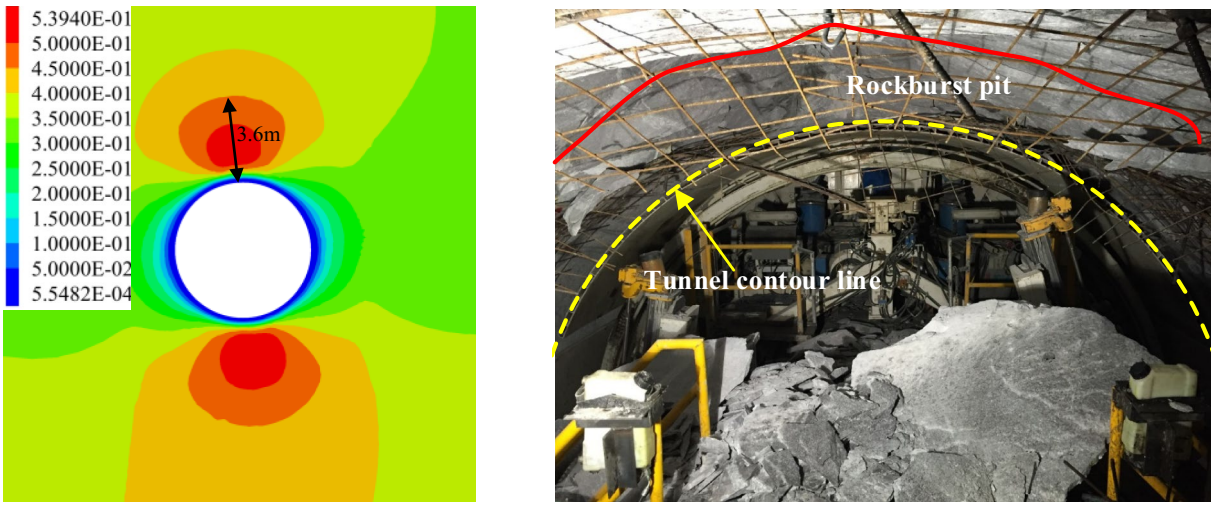

(a) U_e/U_0 distribution (unit: J·m^3)

(b) On-site rockburst

Figure 18. Comparison of rockburst analysis results.

During the actual construction process on site, rockbursts rarely occurred at the right arch bottom, which was mainly due to the influence of the TBM's own weight, which changed the stress distribution near the bottom. It is worth noting that the influence of the TBM's own weight on the surrounding rock stress was not considered in the numerical simulation, but this did not affect the analysis results of other parts.

Conclusion

Through the in-situ stress test and inversion of the deep buried Qinling tunnel crossing the ridge, combined with the dynamic adjustment law of stress and elastic strain energy of the surrounding rock during tunnel excavation, the stress and energy conditions of the rockburst occurred during excavation are proved. The main conclusions are as follows:

1. The maximum principal stress of the deep buried tunnel crossing the ridge of Qinling is 40–66 MPa, which belongs to extremely high in-situ stress level, and medium-strong rockburst may occur during excavation.
2. In the process of TBM excavation, the surrounding rock stress in the range of 3.7 times the diameter of the tunnel before and after the working face is violently adjusted. The concentrated zones after stress redistribution are mainly distributed in the arch roof and arch bottom, and the stress concentration factor can be up to 2.06. The arch roof, arch waist, and arch bottom are susceptible to immediate rockburst due to stress transient unloading at the moment of excavation. The arch roof and arch bottom are susceptible to time delayed rockburst after stress redistribution.
3. The elastic strain energy of the surrounding rock has experienced the process of release and accumulation. The rockburst energy index U_e/U_0 shows the strong rockburst tendency at the arch roof and arch bottom, and the maximum depth of the rockburs pit can reach 3.5 m, which is basically consistent with the location and depth of the rockburst observed in the field.

Data availability

Data will be made available on request and can be obtained by contacting Chao Zhou (email: czhouwhu@whu.edu.cn).

Received: 11 May 2024; Accepted: 2 August 2024
Published online: 05 August 2024

References

1. Siren, T., Kantia, P. & Rinne, M. Considerations and observations of stress-induced and construction-induced excavation damage zone in crystalline rock. *Int. J. Rock Mech. Min.* **73**, 165–174 (2015).
2. Zhao, Z., Tan, Y., Chen, S., Ma, Q. & Gao, X. Theoretical analyses of stress field in surrounding rocks of weakly consolidated tunnel in a high-humidity deep enevironment. *Int. J. Rock Mech. Min.* **122**, 104064 (2019).
3. Xue, T. *et al.* Geo-mechanical model test on the water inrush induced by zonal disintegration of deep tunnel under hydro-mechanical coupling. *Int. J. Rock Mech. Min.* **160**, 105278 (2022).
4. Gao, L. *et al.* Stress distribution characteristics of the surrounding rock of the gob-side coal–rock roadway in a gently inclined coal seam under the influence of excavation and mining disturbance based on infrared detection. *Int. J. Geomech.* **23**(12), 04023233 (2023).
5. Cook, N. G. W. The basic mechanics of rockbursts. *J. S. Afr. Inst. Min. Metall.* **64**(3), 71–81 (1963).
6. Cook, N. G. W. A note on rockbursts considered as a problem of stability. *J. S. Afr. Inst. Min. Metall.* **65**(8), 437–446 (1965).
7. Feng, X. *et al.* Studies on the evolution process of rockbursts in deep tunnels. *J. Rock Mech. Geotech.* **4**(4), 289–295 (2012).
8. Xiao, Y., Feng, X., Li, S. & Yu, Y. Rock mass failure mechanisms during the evolution process of rockbursts in tunnels. *Int. J. Rock Mech. Min.* **83**, 174–181 (2016).
9. Liu, J., Gao, Y., Chen, F. & Cao, Z. Mechanism study and tendency judgement of rockburst in deep-buried underground engineering. *Minerals* **12**, 1241 (2022).
10. He, M. C., Nie, W., Zhao, Z. Y. & Guo, W. H. Experimental investigation of bedding plane orientation on the rockburst behavior of sandstone. *Rock Mech. Rock Eng.* **45**, 311–326 (2012).
11. He, M., Yang, Y., Gao, F. & Fan, Y. Stress sensitivity origin of extended defects production under coupled irradiation and mechanical loading. *Acta Mater.* **248**, 118758 (2023).
12. Fan, Y., Iwashita, T. & Egami, T. Evolution of elastic heterogeneity during aging in metallic glasses. *Phys. Rev. E* **89**(6), 062313 (2014).
13. Fan, Y., Osetskiy, Y. N., Yip, S. & Yildiz, B. Mapping strain rate dependence of dislocation-defect interactions by atomistic simulations. *Proc. Natl. Acad. Sci. USA* **110**(44), 17756–17761 (2013).
14. Fan, Y., Yildiz, B. & Yip, S. Analogy between glass rheology and crystal plasticity: Yielding at high strain rate. *Soft Matter* **9**(40), 9511–9514 (2013).
15. Fan, Y., Osetsky, Y. N., Yip, S. & Yildiz, B. Onset mechanism of strain-rate-induced flow stress upturn. *Phys. Rev. Lett.* **109**(13), 135503 (2012).
16. Bai, Z., Balbus, G. H., Gianola, D. S. & Fan, Y. Mapping the kinetic evolution of metastable grain boundaries under non-equilibrium processing. *Acta Mater.* **200**, 328–337 (2020).
17. Bai, Z. & Fan, Y. Abnormal strain rate sensitivity driven by a unit dislocation-obstacle interaction in bcc Fe. *Phys. Rev. Lett.* **120**(12), 125504 (2018).
18. Tian, L., Fan, Y., Li, L. & Mousseau, N. Identifying flow defects in amorphous alloys using machine learning outlier detection methods. *Scripta Mater.* **186**, 185–189 (2020).
19. Fan, Y., Iwashita, T. & Egami, T. How thermally activated deformation starts in metallic glass. *Nat. Commun.* **5**(1), 5083 (2014).
20. Liu, C., Guan, P. & Fan, Y. Correlating defects density in metallic glasses with the distribution of inherent structures in potential energy landscape. *Acta Mater.* **161**, 295–301 (2018).
21. Fan, Y., Iwashita, T. & Egami, T. Energy landscape-driven non-equilibrium evolution of inherent structure in disordered material. *Nat. Commun.* **8**(1), 15417 (2017).
22. Fan, Y., Iwashita, T. & Egami, T. Crossover from localized to cascade relaxations in metallic glasses. *Phys. Rev. Lett.* **115**(4), 045501 (2015).

23. Fan, Y., Yip, S. & Yildiz, B. Autonomous basin climbing method with sampling of multiple transition pathways: Application to anisotropic diffusion of point defects in hcp Zr. *J. Phys. Condens. Matter.* **26**(36), 365402 (2014).
24. Fan, Y., Kushima, A., Yip, S. & Yildiz, B. Mechanism of void nucleation and growth in bcc Fe: Atomistic simulations at experimental time scales. *Phys. Rev. Lett.* **106**(12), 125501 (2011).
25. Fan, Y., Kushima, A. & Yildiz, B. Unfaulting mechanism of trapped self-interstitial atom clusters in bcc Fe: A kinetic study based on the potential energy landscape. *Phys. Rev. B* **81**(10), 104102 (2010).
26. Zhao, Z., Ali, E., Wu, G. & Wang, X. Assessment of strain energy storage and rock brittleness indices of rockburst potential from microfabric characterizations. *Am. J. Earth Sci.* **2**(8), 32 (2015).
27. Si, X., Luo, Y., Gong, F., Huang, J. & Han, K. Temperature effect of rockburst in granite caverns: Insights from reduced-scale model true-triaxial test. *Geomech. Geophys. Geol.* **10**(1), 26 (2024).
28. Si, X., Luo, Y. & Luo, S. Influence of lithology and bedding orientation on failure behavior of "D" shaped tunnel. *Theor. Appl. Fract. Mech.* **129**, 104219 (2024).
29. Su, G., Ren, H., Jiang, J. & Hu, X. Experimental study on the characteristics of rockburst occurring at the working face during tunnel excavation. *Int. J. Rock Mech. Min.* **164**, 105347 (2023).
30. Wu, W., Gong, F., Ren, L. & He, L. Strain rockburst failure characteristics and mechanism of high stress circular hard rock tunnel triggered by dynamic impact load. *Int. J. Rock Mech. Min.* **171**, 105575 (2023).
31. Li, C. C., Zhao, T., Zhang, Y. & Wan, W. A study on the energy sources and the role of the surrounding rock mass in strain burst. *Int. J. Rock Mech. Min.* **154**, 105114 (2022).
32. Zhu, B., Fan, J., Shi, X., Liu, P. & Guo, J. Study on rockburst proneness of deep tunnel under different geo-stress conditions based on DEM. *Geotech. Geol. Eng.* **40**, 1373–1386 (2022).
33. Qiu, D. *et al.* Rockburst prediction based on tunnel geological exploration and ground stress field inverse analysis. *Rock Soil Mech.* **36**(07), 2034–2040 (2015) (**(in Chinese)**).
34. Liu, F., Zhang, Y. & Ma, T. Rockburst and microseismicity characteristics in the qinling water conveyance tunnel of the hanjiang-to-weihe river diversion project. *Int. J. Rock Mech. Min.* **148**, 104973 (2021).
35. Askaripour, M., Saeidi, A., Rouleau, A. & Mercier-Langevin, P. Rockburst in underground excavations: A review of mechanism, classification, and prediction methods. *Undergr. Space* **7**(4), 577–607 (2022).
36. Lu, J., Gong, Q., Wei, J., Han, B. & Yin, L. Determination of rockburst reduction coefficient β_A in the modified rock mass classification system for TBM tunnels and tunneling. *Int. J. Rock Mech. Min.* **174**, 105657 (2024).
37. The National Standards Compilation Group of People's Republic of China. *GB 50287-2016 Code for Engineering Geological Investigation of Water Resources and Hydropower* 139–140 (China Planning Press, 2016) (**in Chinese**).
38. Chen, W., Lu, S., Guo, X. & Qiao, C. Research on unloading confining pressure tests and rockburst criterion based on energy theory. *Chin. J. Rock Mech. Eng.* **28**(8), 1530–1540 (2009) (**(in Chinese)**).
39. Orlecka-Sikora, B., Lasocki, S., Lizurek, G. & Rudziński, Ł. Response of seismic activity in mines to the stress changes due to mining induced strong seismic events. *Int. J. Rock Mech. Min.* **53**, 151–158 (2012).
40. Wang, G. F. *et al.* Evolution of stress concentration and energy release before rock bursts: Two case studies from Xingan coal mine, Hegang, China. *Rock Mech. Rock Eng.* **49**, 3393–3401 (2016).
41. Zhou, C., Yin, J., Liu, Y., Han, X. & Zhang, X. Inversion analysis of the complex initial stress field of an extra-long tunnel based on "overlapping partition-integration. In *ISRM International Symposium-Asian Rock Mechanics Symposium*. ISRM-ARMS11, ISRM (2021).
42. Zhou, C. *et al.* The partitioned inversion method of initial stress field of extra-long tunnel considering the direction of boundary load. *Chin. J. Rock Mech. Eng.* **41**(S1), 2725–2734 (2022) (**(in Chinese)**).
43. He, M. & Sousa, L.R. Experiments on rock burst and its control. In *Australasian Ground Control in Mining Conference*, *Sidney* 19–31 (2014).
44. Si, X. & Gong, F. Strength-weakening effect and shear-tension failure mode transformation mechanism of rockburst for fine-grained granite under triaxial unloading compression. *Int. J. Rock Mech. Min.* **131**, 104347 (2020).

Acknowledgements

This work was supported by the Major science and technology special plan of Yunnan Province [grant numbers 202002AF080003, 202102AF080001], and the Fundamental Research Funds for the Central public welfare research institutes [grant numbers CKSF2023308/YT, CKSF2023316/YT]. The authors thanks to all supporters.

Author contributions

C.Z.: Writing-original draft, Software, Investigation, Data curation. Z.D.: Conceptualization, Methodology, Funding acquisition, Writing—review & editing. C.Z.: Investigation, Data curation. P.F.: Data curation. S.L.: Investigation, Data curation.

Competing interests

The authors declare no competing interests.

Additional information

Correspondence and requests for materials should be addressed to Z.D.